An Examination of Quasi-Balanced Dynamics in Hurricane Bonnie (1998) using the Invertibility Principle of Ertel's Potential Vorticity

Brian Guyer

A scholarly paper in partial fulfillment of the requirements for the degree of Master of Science

November 2004

Department of Meteorology, University of Maryland

College Park, Maryland 20742

Advisor: Professor Da-Lin Zhang

ABSTRACT

In this study, we examine the quasi-balanced dynamics of Hurricane Bonnie (1998) using the invertibility principle of Ertel's potential vorticity (PV). Given an atmospheric flow that is dynamically balanced, the conservative property of PV (in the absence of heating and friction) may be exploited to obtain a simple interpretation of all relevant dynamical information. Previous studies have shown that the invertibility approach is robust and represents reasonably well many typical features of axisymmetric hurricanes. In our study we will show that the invertibility approach is also useful for describing typical features present in the highly asymmetric case of Hurricane Bonnie (1998). In particular, the partial eyewall and double eyewall stages of Bonnie will be examined. With the aid of the NCAR/PSU mesoscale model (MM5) we will compare the "true" model field to the inverted quasi-balanced field to describe the quasi-balanced features in this highly asymmetric hurricane.

1. Introduction

The invertibility principle of potential vorticity (PV) has become widely used as a diagnostic tool for assessing atmospheric flows. Eliasson and Kleinschmidt (1957) published the first article on the inversion of Ertel's potential vorticity. More detailed articles were then published by Hoskins et al. (1985) and Thorpe (1986). It is the more recent work of Davis and Emanuel (1991) and Davis (1992) that laid the foundation for the inversion system that is used in this study. Davis and Emanuel used the PV approach to diagnose the dynamics of mid-latitude cyclogenesis. They made use of Ertel's PV for their PV equation and the horizontal divergence of the horizontal momentum equations as their balanced condition. In this approach it was assumed that the divergent component was much smaller than the non-divergent component in order to reduce the equations to some balanced state. However, the PV equation and balanced condition are highly nonlinear making the inversion difficult to perform. Due to such strong nonlinearities inherent in those equations the PV approach was linearized. They assumed that PV was positive everywhere to avoid ellipticity problems in the equations when solved. They found that by utilizing the PV approach it was possible to isolate the effects of nonconservative processes on the dynamics (i.e., friction and heating) and quantify their importance in the development of other features.

Since the Davis and Emanuel experiment took place, other important applications of the inversion concept have become known. Wang and Zhang (2003) have shown the PV concept could be used to exploit the unbalanced portion of tropical cyclone flows to study propagating inertial-gravity waves and vortex Rossby waves. However, in their study they abandoned the linearization of Davis and Emanuel and circumvented the

ellipticity requirements in the nonlinear balance equation by developing an equation transformation with the use of a multiplication factor ε. They found that the PV inversion represents reasonably well many typical features of Hurricane Andrew (1992) including; the intense convergent inflow in the planetary boundary layer (PBL) and maximum tangential winds near the top of the PBL, a sloping radius of maximum wind (RMW), a low-level thermal inversion and the warm-core eye, organized updrafts in the eyewall and subsidence in the eye, and upper-level anticyclonic-divergent outflow.

In this study, Wang and Zhang's PV approach is used to examine the quasi-balanced features of Hurricane Bonnie (1998). Unlike the highly axisymmetric case of Hurricane Andrew, Hurricane Bonnie is highly asymmetric during a majority of its lifetime, exhibiting partial eyewall and double eyewall stages. Rogers et. al (2003) showed that vertical wind shear of the environmental flow was a significant factor contributing to the asymmetries present in Bonnie. However, many of the typical features found in symmetric hurricanes, such as those mentioned for Andrew, are also inherent in the circulation structure of Bonnie. In addition, the PV inversion is still capable of reproducing a significant portion of the features of Bonnie and provides detailed information on the quasi-balanced features present suggesting that the inversion system of Wang and Zhang is robust. This study will focus primarily on the partial eyewall and double eyewall stages of Bonnie since it is desirable to see to what extent the conclusions made in Wang and Zhang are applicable.

The next section will discuss the model specifications used to provide data for the study. Section 3 will outline the formulation of the PV inversion system adopted from Wang and Zhang (2003). Section 4 will discuss quasi-balanced flows present during the

partial eyewall and double eyewall periods. Finally, section 5 will include some concluding remarks.

2. Model Description

The latest version of the PSU/NCAR nonhydrostatic, two-way interactive, movable, triply nested mesoscale model (MM5V3.4, Dudhia 1993 and Grell et al. 1995) along with the potential vorticity inversion system used in Wang and Zhang (2003) will be employed to examine Hurricane Bonnie (1998). The model design is similar to that used in Zhu et al. (2003) and Liu et al. (1997). The model physics include the Tao-Simpson (1993) cloud microphysics scheme, the Kain-Fritsch (1993) convective parameterization, the Blackadar PBL scheme (Zhang and Anthes 1982), and a cloud-radiation interaction scheme. The initial conditions and lateral boundary conditions are from the NCEP 2.5°x2.5° global analyses that are then enhanced by rawinsondes and surface observations. The mass and wind fields used to bogus the vortex are from the Advanced Microwave Sounding Unit-A (AMSU-A) data because the NCEP global analysis vortex was 12hPa too weak. The sea surface temperature was updated daily using Tropical Rainfall Measuring Mission (TRMM) Microwave Imager (TMI) Level-1 standard level-products on a 0.25°x0.25° latitude/longitude resolution.

Table 1 outlines the grid system of the hurricane model. The data used for this study is from the finest mesh domain (Δ=4 km) of a 5-day simulation of Hurricane Bonnie (1998) initiated on 0000 UTC 22 August. The finest domain was initiated 12 hours later on 1200 UTC 22 August and continues for 108 hours ending at 0000 UTC 27 August. This study examines a portion of the finest domain beginning on 0000 UTC 24

August and ending at 1500 UTC 25 August because the partial eyewall and double eyewall stages of Bonnie are most prominent during this period. The grid consists of 163x163 horizontal grid points spanning 648x648 km. The grid was then reduced to 161x161 points to on each side of the domain to avoid any spurious boundary values encroaching from the medium resolution domain. The vertical resolution of the model consists of 24-sigma levels and preserves the greatest resolution in the planetary boundary layer. Model variables are output on an Arakawa-B staggered grid. The finest mesh domain moves automatically with the column averaged maximum relative vorticity every six hours.

3. Formulation

The subsequent PV inversion diagnostic programming package consists of two parts. First, the gradient wind balanced reference state (mean) flow fields and the model representative total flow fields are prepared by performing Fourier series decompositions at wavenumber-0 and wavenumber-6, respectively. To perform the Fourier decomposition the model rectangular coordinates are transformed into cylindrical coordinates with the minimum sea surface pressure defining the center. The perturbation flow fields are defined by subtracting the mean flow fields from the total flow fields. Secondly, a system of elliptic partial differential equations are developed, using the PV equation and a nonlinear balanced condition, and solved using the multigrid software MUDPACK (Adams 1993) to obtain the 3D quasi-balanced flow fields. To perform the inversion with MUDPACK it is necessary that the grid dimensions are square and that the vertical resolution is even. The uneven 24-sigma levels are interpolated to 33 even

vertical levels and the horizontal grid size is reduced to 97x97 to encourage the computational efficiency of MUDPACK. Since the eyewall diameter reaches nearly 200 km the reduced grid size is still suitable for this study and will provide sufficient detail for examining the partial eyewall and double eyewall stages of Bonnie. A detailed outline of the diagnostic formulation for the inversion can be found in Wang and Zhang (2003).

A general form of Ertel's potential vorticity is used to obtain the spatial distribution of PV,

$$Q = \frac{1}{\rho}\vec{\eta} \cdot \nabla\theta_\rho \qquad (1)$$

where ρ is the total density including dry air, moisture, and precipitation; $\vec{\eta} = 2\vec{\Omega} + \nabla \times \vec{V}$ is the absolute vorticity vector, and θ_ρ is the virtual potential temperature. The horizontal wind $\vec{V}_h$ is decomposed into nondivergent and irrotational components by defining a streamfunction ψ and a velocity potential χ,

$$\vec{V}_h = \nabla\psi \times \vec{k} + \nabla\chi = \vec{V}_\psi + \vec{V}_\chi . \qquad (2)$$

The LaPlacian's of the streamfunction and the velocity potential define the vorticity ς and the divergence D respectively,

$$\nabla^2\psi = \vec{k} \cdot \nabla \times \vec{V}_h = \varsigma \quad \text{and} \quad \nabla^2\chi = \nabla \cdot \vec{V}_h = D . \qquad (3)$$

To develop the NLB equation the divergence operator is applied to the equations of motion in component form and the hydrostatic assumption and nondivergent assumption, $\left|\vec{V}_\chi\right| << \left|\vec{V}_\psi\right|$, are applied to obtain,

$$\nabla_h^2\phi = \nabla_h \cdot (f\nabla\psi) + 2J(\frac{\partial\psi}{\partial x}, \frac{\partial\psi}{\partial y}) + \nabla_h \cdot \vec{f}_r \qquad (4)$$

$$q = [(f + \nabla^2\psi)\frac{\partial^2\phi}{\partial z^2} + \frac{\partial^2\psi}{\partial x\partial z}\frac{\partial^2\phi}{\partial x\partial z} + \frac{\partial^2\psi}{\partial y\partial z}\frac{\partial^2\phi}{\partial y\partial z}] \qquad (5)$$

where $z = (1 - \pi / c_p)z_a$, $\pi = c_p(p/p_0)^{\frac{R_d}{c_p}}$ is the vertical coordinate used for the study defined by Davis and Emanuel (1991), $z_a = c_p\theta_0/g$, J is the Jacobian operator, f is the Coriolis parameter, $\vec{f}_r$ is the friction vector, ϕ is the geopotential, ψ is the streamfunction, and q is the known distribution of PV from the mesoscale model output. The frictional tendencies were calculated separately from the MM5 output using an implicit diffusion scheme. Equations (4) and (5) are then linearized by

$$\psi' = \psi - \overline{\psi} \qquad \phi' = \phi - \overline{\phi} \qquad q' = q - \overline{q}\,. \qquad (6)$$

The resulting set of equations become,

$$\nabla_h^2\phi' = f\nabla_h^2\psi' + \beta\frac{\partial\psi'}{\partial y} + 2(\frac{\partial^2\overline{\psi}}{\partial x^2}\frac{\partial^2\psi'}{\partial y^2} - 2\frac{\partial\overline{\psi}}{\partial x\partial y}\frac{\partial\psi'}{\partial x\partial y} + \frac{\partial\psi'}{\partial x^2}\frac{\partial\overline{\psi}}{\partial y^2}) + 2[\frac{\partial^2\psi'}{\partial x^2}\frac{\partial\psi'}{\partial y^2} - (\frac{\partial\psi'}{\partial x\partial y})^2] + \frac{\partial f_x}{\partial x} + \frac{\partial f_y}{\partial y}, \qquad (7)$$

and

$$q' = (f + \nabla_h^2\overline{\psi})\frac{\partial^2\phi'}{\partial z^2} + \nabla_h^2\psi'\frac{\partial\overline{\phi}}{\partial z^2} - \frac{\partial^2\overline{\psi}}{\partial x\partial z}\frac{\partial\phi'}{\partial x\partial z} - \frac{\partial^2\psi'}{\partial x\partial z}\frac{\partial\overline{\phi}}{\partial x\partial z} - \frac{\partial^2\overline{\psi}}{\partial y\partial z}\frac{\partial\phi'}{\partial y\partial z} - \frac{\partial^2\psi'}{\partial y\partial z}\frac{\partial\overline{\phi}}{\partial y\partial z} + \nabla_h^2\psi'\frac{\partial\phi'}{\partial z^2} - \frac{\partial^2\psi'}{\partial x\partial z}\frac{\partial\phi'}{\partial x\partial z} - \frac{\partial^2\psi'}{\partial y\partial z}\frac{\partial\phi'}{\partial y\partial z}. \qquad (8)$$

They are solved using MUDPACK with the appropriate lateral, top, and bottom boundary conditions. Once these nonlinear balance equations are solved the new iterated streamfunction and geopotential perturbations are then added back to the reference state to obtain a new total balanced streamfunction and geopotential.

Once the 3D balanced mass and wind fields are obtained the divergent component, V_Ψ, is considered because of its importance to the contribution of the secondary circulation (Wang and Zhang 2003). The secondary circulation is determined by using an ω- equation and a mass continuity equation. Given the following vorticity equation,

$$\frac{\partial \zeta}{\partial t} = -(\vec{V}_\psi + \vec{V}_\chi)\cdot\nabla_h\eta - \omega\frac{\partial \eta}{\partial z} - \eta\nabla_h\cdot\vec{V}_\chi + \frac{\partial \omega}{\partial y}\frac{\partial u}{\partial z} - \frac{\partial \omega}{\partial x}\frac{\partial v}{\partial z} + \frac{\partial f_x}{\partial x} + \frac{\partial f_y}{\partial y} \tag{9}$$

and the thermodynamic equation,

$$\frac{\partial \theta_\rho}{\partial t} + u\frac{\partial \theta_\rho}{\partial x} + v\frac{\partial \theta_\rho}{\partial y} + \omega\frac{\partial \theta_\rho}{\partial z} = \dot{q}_\rho \tag{10}$$

where $\dot{q}_\rho$ is the heating rate including moisture effects, and it is assumed that the Eulerian derivative part can be neglected, we can form the ω- equation. Performing $g/\theta_0\,(10) - \partial^2(4)/\partial t\partial z - f\partial(9)/\partial z$ and some manipulation we obtain the quasi-balanced ω-equation,

$$\begin{aligned}
&\nabla_h^2\left(\frac{\partial^2\phi}{\partial z^2}\omega\right) + f\eta\frac{\partial}{\partial z}\{(z_a - z)^{-\mu}\frac{\partial}{\partial z}[(z_a - z)^\mu\omega]\} - f\frac{\partial}{\partial z}\left(\frac{\partial \omega}{\partial x}\frac{\partial^2\psi}{\partial x\partial z} + \frac{\partial \omega}{\partial y}\frac{\partial^2\psi}{\partial y\partial z}\right)\\
&- f\frac{\partial}{\partial z}\left(\frac{\partial \omega}{\partial x}\frac{\partial^2\chi}{\partial x\partial z} + \frac{\partial \omega}{\partial y}\frac{\partial^2\chi}{\partial y\partial z}\right) - \left(f\frac{\partial \eta}{\partial z}\frac{\mu}{z_a - a} + f\frac{\partial^2\eta}{\partial z^2}\right)\omega\\
&= f\frac{\partial}{\partial z}[\vec{V}_h\cdot\nabla\eta] - \nabla_h^2[V_h\cdot\nabla_h\frac{\partial\phi}{\partial z}] - 2\frac{\partial^2}{\partial t\partial z}\left(\frac{\partial^2\psi}{\partial x^2}\frac{\partial^2\psi}{\partial y^2} - \frac{\partial^2\psi}{\partial x\partial y}\frac{\partial^2\psi}{\partial x\partial y}\right)\\
&- \beta\frac{\partial^3\psi}{\partial t\partial y\partial z} + \frac{g}{\theta_0}\nabla_h^2\dot{q}_\rho - f\frac{\partial}{\partial z}\left(\frac{\partial f_y}{\partial x} - \frac{\partial f_x}{\partial y}\right) - \frac{\partial^2}{\partial t\partial z}\left(\frac{\partial f_y}{\partial x} + \frac{\partial f_x}{\partial y}\right)
\end{aligned} \tag{11}$$

where $\mu = c_v/R_d$, ψ and ϕ are the total streamfunction and geopotential from equations (7) and (8). We neglect the last term on the right hand side of equation (11) because there was no tendency output for friction from the MM5 and it is reasonably small.

However, including this term may result in a more accurate representation of the vertical velocity field. Since the LaPlacian of the velocity potential, χ, is related to the divergence from equation (3), it can be found by forming a continuity equation with omega,

$$\nabla^2 \chi = -(z_a - z)^{-\mu} \frac{\partial}{\partial z}[(z_a - z)^{\mu} \omega]. \qquad (12)$$

Since equation (12) represents the irrotational portion of the horizontal wind, it can be added to the nondivergent component obtained from equations (7) and (8) to yield the total horizontal wind field. This is then substituted into the vorticity equation to obtain the streamfunction tendency for the third term on the RHS of equation (11). Therefore, equations (9), (10), and (11) in addition to the linearized forms of equation (7) and (8) define a complete 3D quasi-balanced flow field through $q, \phi, \psi, \omega,$ and χ.

In all, with a known 3D distribution of PV from the model output, it is possible to obtain the quasi-balanced mass and wind fields using the NLB equation. These results are then compared to the model representative fields to examine the quasi-balanced features in the following section.

4. Quasi-Balanced Flows

In this section, the inverted quasi-balanced mass and wind fields are verified against the model simulated mass and wind fields for the partial eyewall and double eyewall stages of Hurricane Bonnie. Figure 1 compares the inverted PV to the PV obtained from the model simulation. The in-plane flow vectors are superimposed along with the radar reflectivity. The melting level is indicated by the 0° isotherm near 6 km. It is evident from the distribution of radar reflectivity that there are significant

asymmetries present across the entire width of the storm. This wavenumber-1 pattern describes well the asymmetric structure of the partial eyewall stage. The eastern eyewall is associated with an intense updraft and upper-level outflow. The western eyewall is associated with a downdraft due to entrainment of cool, dry environmental air. The pattern of PV is slantwise to the east with several local maximums. There are two maximums of PV surrounding the eye region near 1 km and another located near 5 km along the western eyewall. The PV maximum near 1 km along the western eyewall may be associated with intense vertical wind shear as can be seen by the in-plane flow vectors. The PV maximum near 5km along the western eyewall may be associated with the broad region of diabatic cooling as can be seen by the shadings in Figure 4. A band of PV greater than 10 PVU is located 120 km to the east of the eye near 7 km. This is associated with rotational shear in a primary spiral rainband. It is encouraging that the inverted PV shows these features even in the presence of such high asymmetry. The difference field is most notable along the surface underneath the western eyewall and near the model top. The large amount of wind shear present in those regions may be a possible source for such large differences.

Figure 2 compares the distribution of tangential winds from the model simulation to the inverted. The RMW is located just outside the intense updraft in the eastern eyewall and within the downdraft in the western eyewall. There is a pair of maximums in the western eyewall region despite the absence of an intense updraft. It is interesting that the wedge of decreased tangential wind near 2 km between the two maximums is located in the same region as the wedge of greater PV discussed in Figure 1. It is evident that the vertical shear is responsible for these features. The inverted field suitably represents the

primary circulation over the eastern half of the storm. However, the difference field at the top of the PBL in the outflow jet region is nearly 15 m s^{-1}. It is evident from the inverted field that the sloping RMW in that region is not as well recovered suggesting the presence of supergradient flow. This feature is also evident in the western eyewall but is limited to only a small layer near 2 km. The difference field shows nearly a 20 m s^{-1} anticylconic perturbation in the PBL near 150 km. This is associated with the lack of a high resolution description of the frictional effects in the PBL. The in-plane flow vectors show that the inversion recovers the upper-level inflow centered near 12 km over the western half of the storm. The difference field pattern above the western portion of the storm near 12 km suggests the presence of an upper-level cyclonic circulation perturbation.

The environmental flow is easily seen over the western portion of the storm in Figure 3. The deep layer inflow from 5 km to the model top in the model simulation is a tremendous factor for the absence of convection along the western eyewall. The upper-level radial inflow near 10 km above the western eyewall is greater than the low-level inflow in the PBL beneath the eastern eyewall. The inverted radial winds in the upper-level inflow region are greater than that in the model simulation. The large difference as seen in panel (c) suggests the upper-level flow in that region is strongly subgradient. In fact, the inverted radial winds are in general too strong in the upper levels over all of Bonnie, whereas they are too weak in the PBL, suggesting that the radial flow associated with the divergent component of the wind field is highly unbalanced.

Figure 4 shows the distribution of vertical velocity superimposed with the total diabatic heating. In this illustration the wavenumber-1 characteristic of the partial

eyewall is obvious. The downdrafts occurring over the western eyewall are well correlated with the latent cooling in the region. The sloping updraft in the eastern eyewall is quite large and is primarily associated with the intense inflow of high ϑ_e air in the PBL as well as the conservation of absolute angular momentum (AAM). By conservation of AAM, the inflow reaches close to the eye and is forced upwards by intense tangential winds [Fig. 2]. The difference field shows that only 50-60% of the model vertical motion in the main updraft core is recovered in the inversion. This underestimation is also notable in Figure 5 of Wang and Zhang (2003). It is also evident that there is a secondary maximum in the vertical motion near 90 km to the east of the eye region. This is the first sign of a developing double eyewall.

Figure 5 compares the model potential temperature deviations to the inverted. The potential temperature deviation is defined as the difference between the actual potential temperature field and the mean potential temperature at each vertical level. There are two maximum potential temperature deviations. One is located at 6 km above the eye region and is the result of a thermal inversion located in that region. This maximum correlates well with the melting level indicated by the 0° isotherm. It can also be seen that the melting level corresponds well with the upper limit of significant precipitation noted by the radar reflectivity. Figure 8a in Zhu and Zhang (2004) shows the existence of a bright band radar reflectivity signature in this region as well. The other maximum potential temperature deviation is located at 14 km and may result from the vertical heat transport by intense vertical motion along the eastern eyewall. It is evident from the flow vectors in that region that there is an area of downward motion along the inner edge of the eyewall in the direction opposite to the upper-level outflow. The

vertical velocity field for the 87-h integration is much less intense and Figure 10 shows no secondary maximum in potential temperature deviation above 7 km.

Figure 6 compares the model PV to the inverted for the 87-h integration. The model simulated and inverted flow fields show a more U-shaped PV structure similar to that noted by Wang and Zhang (2003). It is evident from the radar reflectivity that there exist two maximums in precipitation associated with two RMWs. The melting level corresponds well with the top of the significant convection in the double eyewall rainbands. There is a PV maximum along the eastern eyewall that compares more favorably to that of Wang and Zhang (2003). The inner-core structure of the PV seems to be uneffected by the existence of the double eyewall structure and is related more to the inner-core dynamics. The inverted in-plane flow vectors struggle to represent the vertical motion near the two maximums in convection in the eastern region. However, the in-plane flow vectors represent more accurately the vertical motion in the western region below 10 km. The difference field shows this large unbalanced westerly wind emanating from the top of the first convective band in the eastern eyewall. Again, these flow features do not seem to effect the distribution of PV. The axes of maximum PV in each convective rainband are well represented by the inversion for the two rainbands east and west of the eye region. As in Figure 1, the melting level nearly intersects the center of the maximums of PV for each spiral rainband.

The model primary circulation is compared to the inverted primary circulation in Figure 7 for the same period. The inner RMW has expanded outward to around 70 km both east and west. It is also evident that the double eyewall structure is associated with the two RMWs. The inversion represents well the primary circulation of the double

eyewall stage. The unbalanced features in the PBL are similar to those present during the partial eyewall stage except they are less impressive. The difference field shows a broad region of tangential winds nearly 10 m s^{-1} greater in the model than in the inverted field. This is a result of the inversion reproducing a broader eye structure so the associated tangential winds are weaker in this region. Also, the globally inverted field misrepresents the small scale features present near 8 km.

The comparison between the model radial flow and the inverted radial flow are shown in Figure 8. Similarly to Figure 7, the difference field in the radial winds is much less pronounced during the double eyewall stage. The differences are about half the magnitude as in the partial eyewall case suggesting that the horizontal wind field associated with the wavenumber-2 double eyewall stage of Bonnie may be more balanced than the waveumber-1 partial eyewall stage. The difference field in panel (c) shows a highly unbalanced feature above the inner-eastern eyewall. The flow vectors show that the source region for this feature is likely associated with the strong outflow induced above the inner-western eyewall. The radial outflow emanating from the top of the inner-western eyewall inhibits the development of vertical motion along the inner-eastern eyewall. The radial winds during the double eyewall stage seem to be in closer agreement to the model simulation however, the vertical motion field is still significantly unbalanced as seen in Figure 9.

Figure 9 compares the model vertical velocity to the inverted vertical velocity. The pattern of diabatic heating correlates well with the patterns of vertical motion except near the inner-eastern eyewall. The differences between the inversion and the model simulation are the same order of magnitude as the model vertical velocity. This again

shows that the vertical velocity is significantly unbalanced in that region. It is unclear whether this strong imbalance is a real feature of that it is due to the frictional effects in the PBL. It is a logical conjecture that since the inversion represents well the other regions of vertical velocity in the double eyewall stage, as well as in the partial eyewall stage, that this feature in indeed highly unbalanced. A future study is needed to determine whether this is a significant source region for propagating waves or there is a problem with the inversion formulation associated with the requirement of non-negative absolute vorticity as mentioned in Wang and Zhang (2003).

Finally, Figure 10 illustrates the potential temperature deviations for the double eyewall stage. As opposed to Figure 5, the core of maximum potential temperature deviations occurs only in the thermal inversion layer above the eye, agreeing with that of Figure 8 in Wang and Zhang (2003). However, in the case of Hurricane Bonnie the deviations are not as large. The difference field is also smaller than the partial eyewall stage. As in Figure 5, the maximum potential temperature deviation is located above the eye near the 0° isotherm. Other pronounced differences occur along the inner-eastern eyewall and near the surface inside the inner-western eyewall.

5. Conclusions

The invertibility approach to examining the quasi-balanced features of Hurricane Bonnie suitably represents the partial eyewall and double eyewall stages. The effects of friction in the PBL are a significant contributing factor in the recalculation of the model storm. Wang and Zhang (2003) pointed out that errors in the representation of the frictional forcing may be to blame for some of the unbalanced features. Since we have

used a different approach for calculating the frictional tendencies than that represented by the MM5 for the Wang and Zhang study, it is very possible that the inversion results obtained in this study could be different. On the other hand, this may help understand the importance of the non-conservative processes of friction since they have been obtained in more than one manner. In all, this study provides insight into the quasi-balanced dynamics of asymmetric hurricanes and proves that the inversion approach is robust.

References

Adams, John C., 1993: MUDPACK-2: Multigrid software for approximating elliptic partial differential equations on uniform grids with any resolution. *Appl. Math. & Comp.*, **53**, 235-249.

Davis, C. A., 1992: Piecewise potential vorticity inversion. *J. Atmos. Sci.*, **49**, 1397-1411.

-------, K. A. Emanuel, 1991: Potential vorticity diagnostics of cyclogenesis. *Mon. Wea. Rev.*, **119**, 1929-1953.

Dudhia, J., 1993: A nonhydrostatic version of the Penn State-NCAR mesoscale model: Validation tests and simulation of an Atlantic cyclone and cold front. *Mon. Wea. Rev.*, **121**, 1493-1513.

Eliasson, A., and E. Kleinschmidt, 1957: Dynamic Meteorology. *Handbuch der Physik*, Vol 48, Springer Verlag, 1-154

Grell, G.A., J. Dudhia, and D. R. Stauffer, 1995: A description of the fifth generation Penn State/NCAR mesoscale model (MM5). NCAR Tech Note NCAR/TN-398+STR, 138 pp. [Available from NCAR Publications Office, P. O. Box 3000, Boulder, CO 80307-3000.]

Hoskins, B. J., M. E. McIntyre and A. W. Robertson, 1985: On the use and significance of isentropic potential vorticity maps. *Quart. J. Roy. Meteor.* Soc., **111**, 877-946.

Kain, L. S., and J. M. Fritsch, 1993: Convective parameterization for mesoscale models: The Kain-Fritsch scheme. *The Representation of Cumulus Convection in Numerical Models, Meteor. Monogr.*, No. 46, Amer. Meteor. Soc., 165-170.

Liu, Y., D.-L. Zhang and M. K. Yau, 1997: A multiscale numerical study of Hurricane Andrew (1992). Part II: Kinematics and inner-core structures. *Mon. Wea. Rev.*,

127, 2597-2616.

Rogers, R. E., S. S. Chen, J. E. Tenerelli, and H. Willoughby, 2002: A numerical study of the impact of vertical shear on the distribution of rainfall in Hurricane Bonnie (1998). Submitted to *Mon. Wea. Rev*.

Tao, W.-K., and J. Simpson, 1993: The Goddard cumulus ensemble model. Part I: Model description. *Terr. Atmos. Oceanic Sci*., **4**, 35-72.

Thorpe, A. J., 1986: Synoptic scale disturbances with circular symmetry. *Mon. Wea. Rev*., **101**, 573-592.

Wang, X. and D.-L. Zhang, 2003: Potential vorticity diagnosis of a simulated hurricane. Part I: Formulation and Quasi-balanced flow. *Mon. Wea. Rev*., ?, ?

Zhang, D.L., R. A. Anthes, 1982: A high-resolution model of the planetary boundary layer- sensitivity test and comparisons with SESAME-79 data. *J. Appl. Meteor*., **21**, 1594-1609.

Zhu, T. and D.-L. Zhang, 2002: Numerical simulation of Hurricane Bonnie (1998). Part I: Eyewall evolution and intensity changes. *Mon. Wea. Rev*., ?, ?

Figure Captions

Table 1. Grid system of the triply nested mesh hurricane model.

Figure 1. West-East vertical cross section of PV (contoured), superimposed with storm-relative in-plane flow vectors, from (a) the model output (every 5 PVU); (b) the inverted or re-calculated (every 5 PVU); and (c) the differences (every 5 PVU) between (a) and (b) [i.e., (a) minus (b)]. They are obtained by averaging three points across the section from the 48-h integrations. Shadings denote the simulated radar reflectivity greater than 15, 25, 35, and 45 dBz that roughly represents the distribution of precipitation with two different intensities. Dashed 0° C contour near 6 km represents the melting level. Solid (dashed) lines are for positive (negative) values. Note that vertical velocity vectors have been amplified by a factor of 5.

Figure 2. As in Figure 1, but for tangential winds at intervals of 5 m s^{-1} in (a), (b), and (c). Solid (dashed) lines denote tangential flows [in (a) and (b)] or their differenced flows [in (c)] into (out of) the page.

Figure 3. As in Figure 1, but for radial winds at intervals of 5 m s^{-1}.

Figure 4. As in Figure 1, but for vertical motions at intervals of 1 m s^{-1}. Light shadings denote latent heating rates greater than 10, 30, and 50 K h^{-1}, whereas dark shadings denote latent cooling rates less than -1 and -5 K h^{-1}.

Figure 5. As in Figure 1, but for potential temperature deviations ϑ' at intervals of 2° C in (a), (b), and (c).

Figure 6. As in Figure 1, but for PV from the 87-h integration. Note the vertical velocity vectors have been amplified by a factor of 10.

Figure 7. As in Figure 6, but for the tangential winds at intervals of 5 m s^{-1} in (a) and (b); and 2.5 m s^{-1} in (c).

Figure 8. As in Figure 6, but for radial winds at intervals of 5 m s^{-1}.

Figure 9. As in Figure 6, but for vertical motions at intervals of 0.2 m s^{-1}. Light shadings denote latent heating rates greater than 5, 10, and 15 K h^{-1}, whereas dark shadings denote latent cooling rates less than -1.5 K h^{-1} and -3.0 K h^{-1}.

Figure 10. As in Figure 6, but for potential temperature deviations ϑ' at intervals of 2° C in (a) and (b); and 1° C in (c).

Table 1. Grid system of triply nested mesh hurricane model

Mesh	Resolution (km)	Grid Size (km)	Time Step (min)
1	36	180x142	1.5
2	12	184x202	0.5
3	4	163x163	180

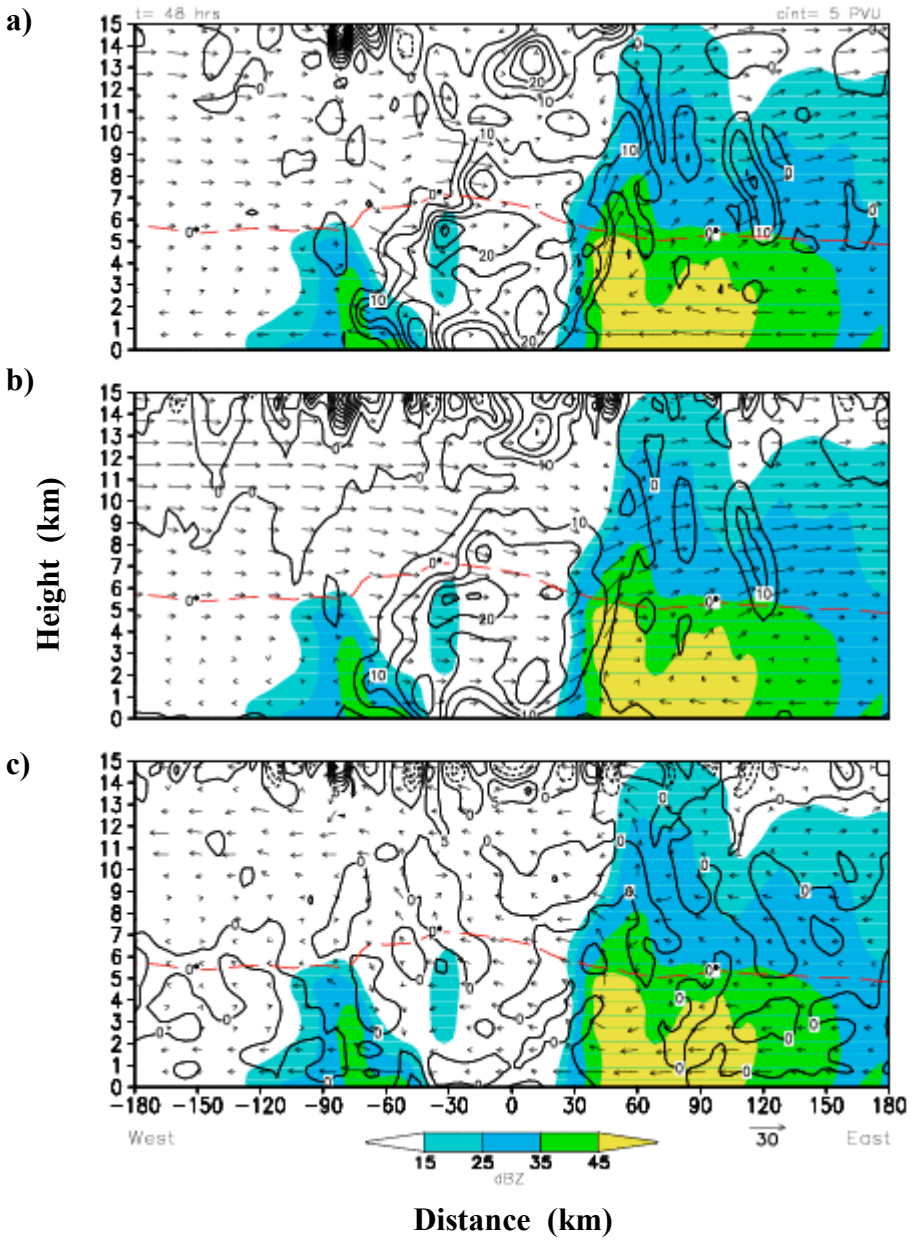

Figure 1. West-East vertical cross section of PV (contoured), superimposed with in-plane flow vectors, from (a) the model output (every 5 PVU); (b) the inverted or re-calculated (every 5 PVU); and (c) the differences (every 5 PVU) between (a) and (b) [i.e., (a) minus (b)]. They are obtained by averaging three points across the section from the 48-h integration. Shadings denote the simulated radar reflectivity greater than 15, 25, 35, and 45 dBz which represent roughly the distribution of precipitation with four different intensities. Dashed 0° C contour near 6 km indicates the melting level. Solid (dashed) lines are for positive (negative) values. Note that the vertical velocity vectors have been amplified by a factor of 5.

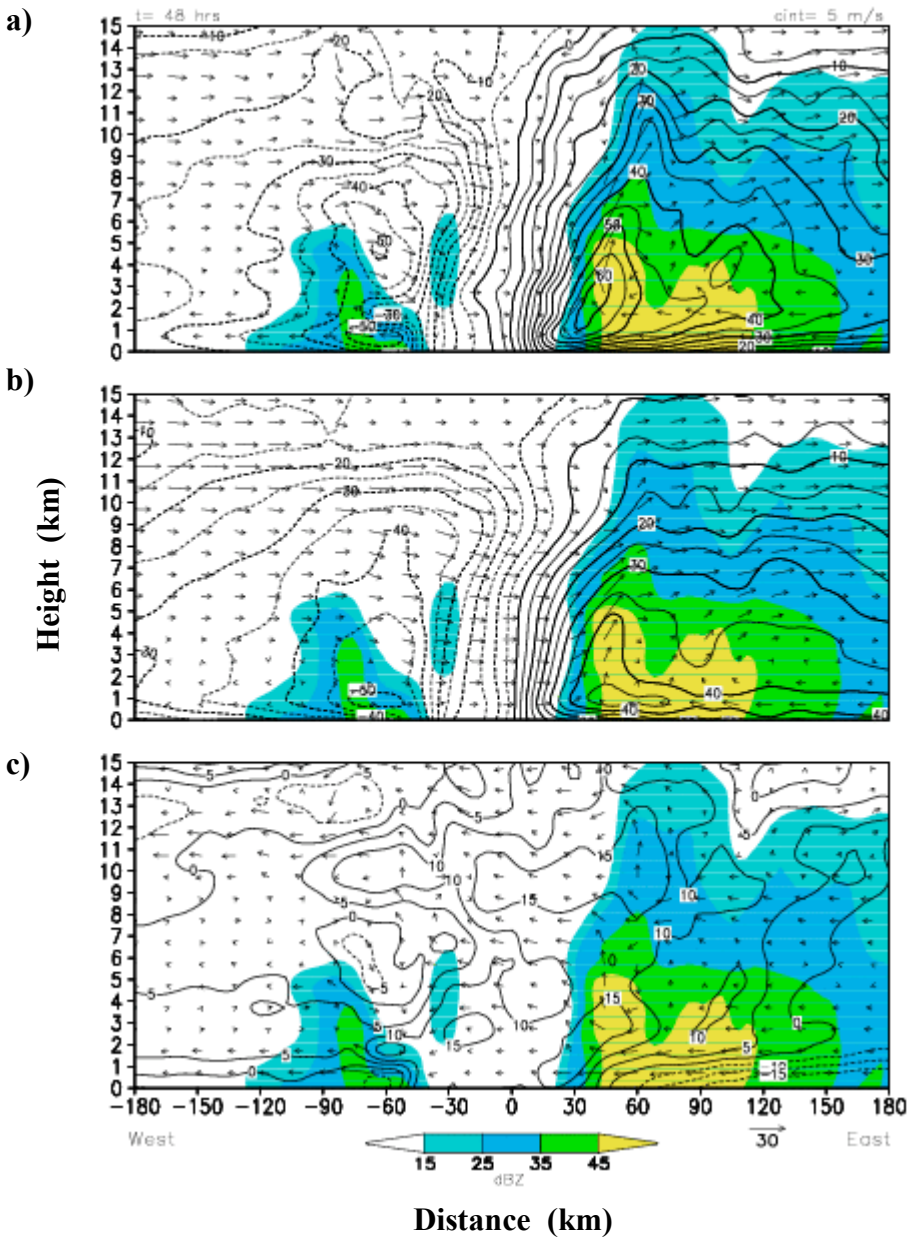

Figure 2. As in Figure 1, but for tangential winds at intervals of 5 m s^{-1} in (a), (b), and (c). Solid (dashed) lines denote tangential flows [in (a) and (b)] or the differenced flows [in (c)] into (out of) the page.

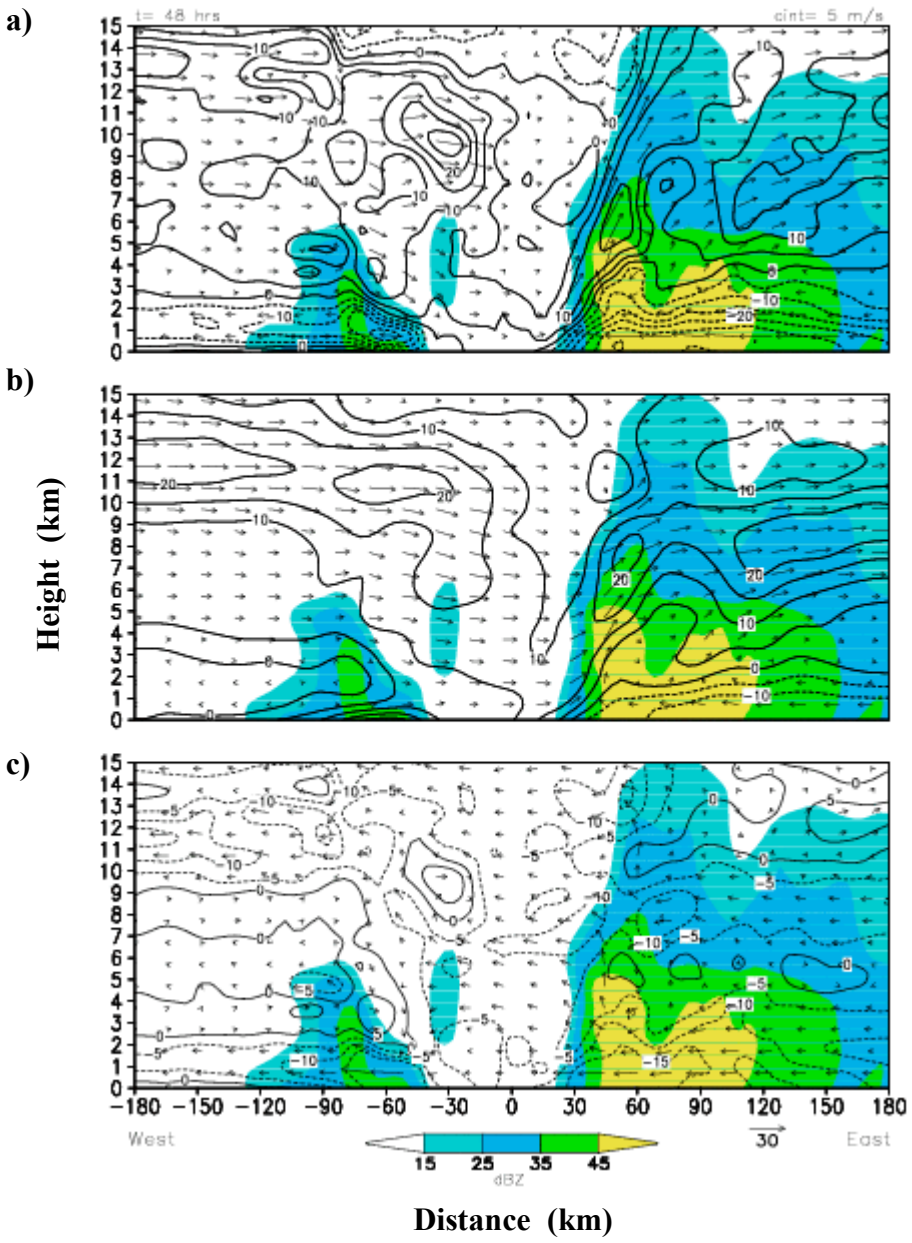

Figure 3. As in Figure 1, but for radial winds at intervals of 5 m s^{-1}.

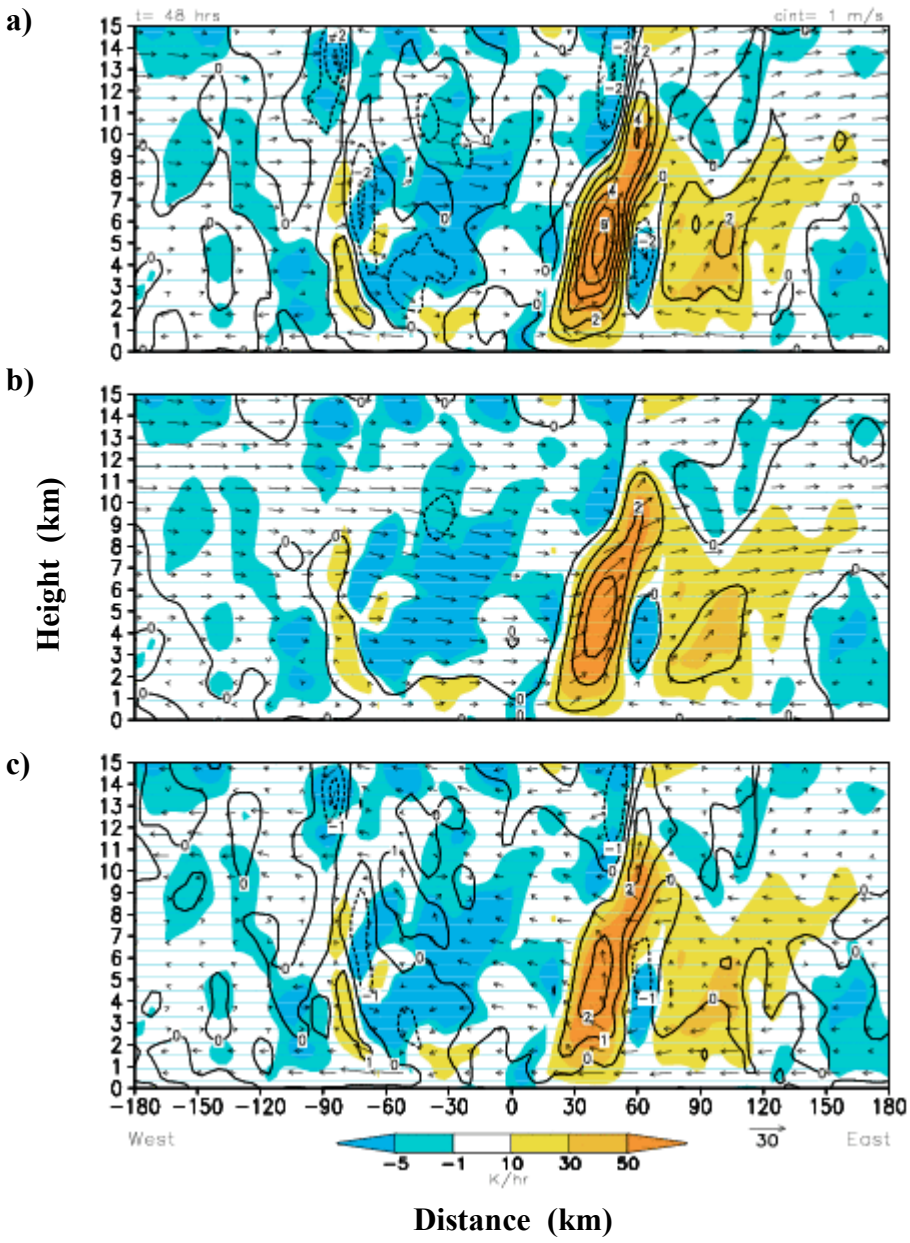

Figure 4. As in Figure 1, but for vertical motions at intervals of 1 m s^{-1}. Light shadings denote latent heating rates greater than 10, 30, and 50 K h^{-1}, whereas dark shadings denote latent cooling rates less than -1 and -5 K h^{-1}.

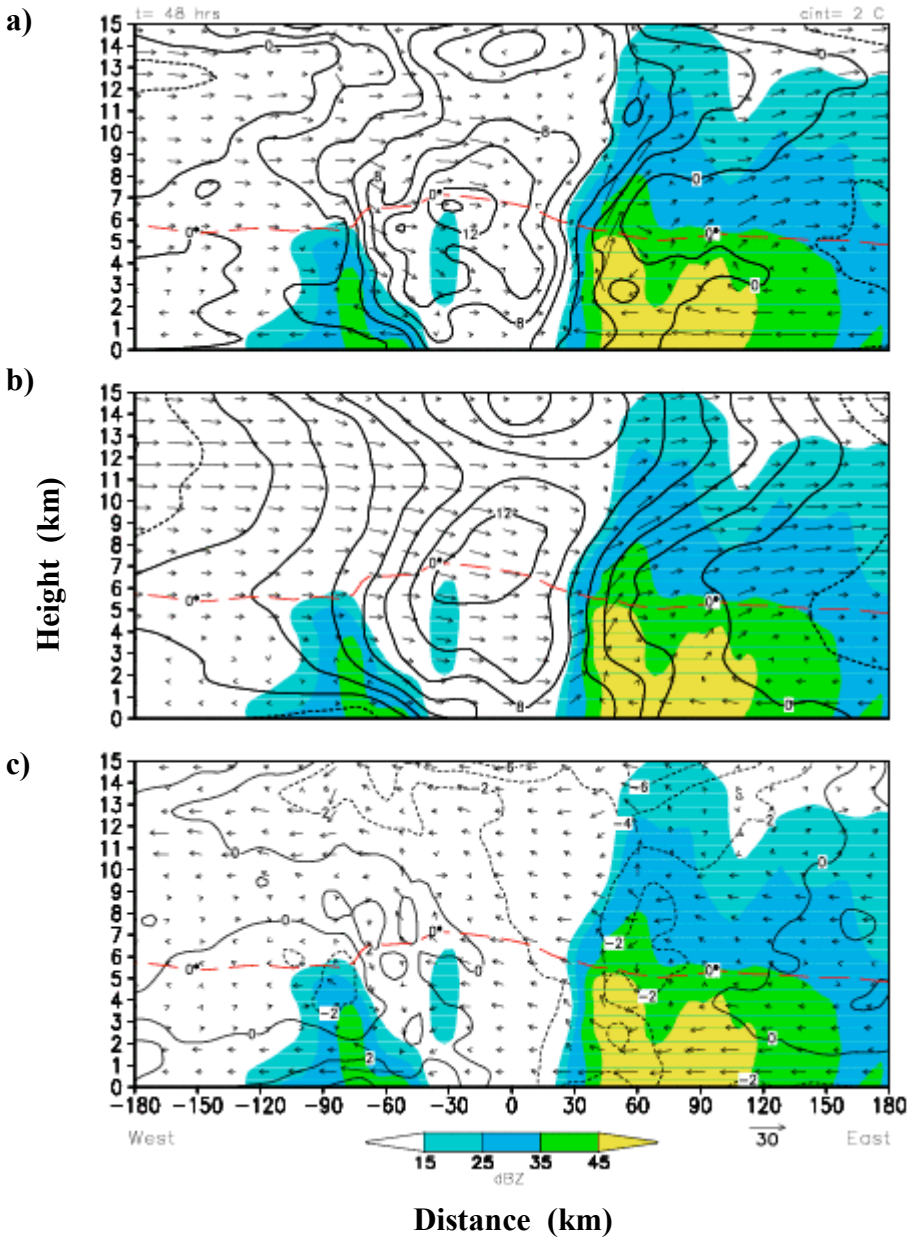

Figure 5. As in Figure 1, but for potential temperature deviations at intervals of 2° C in (a), (b), and (c).

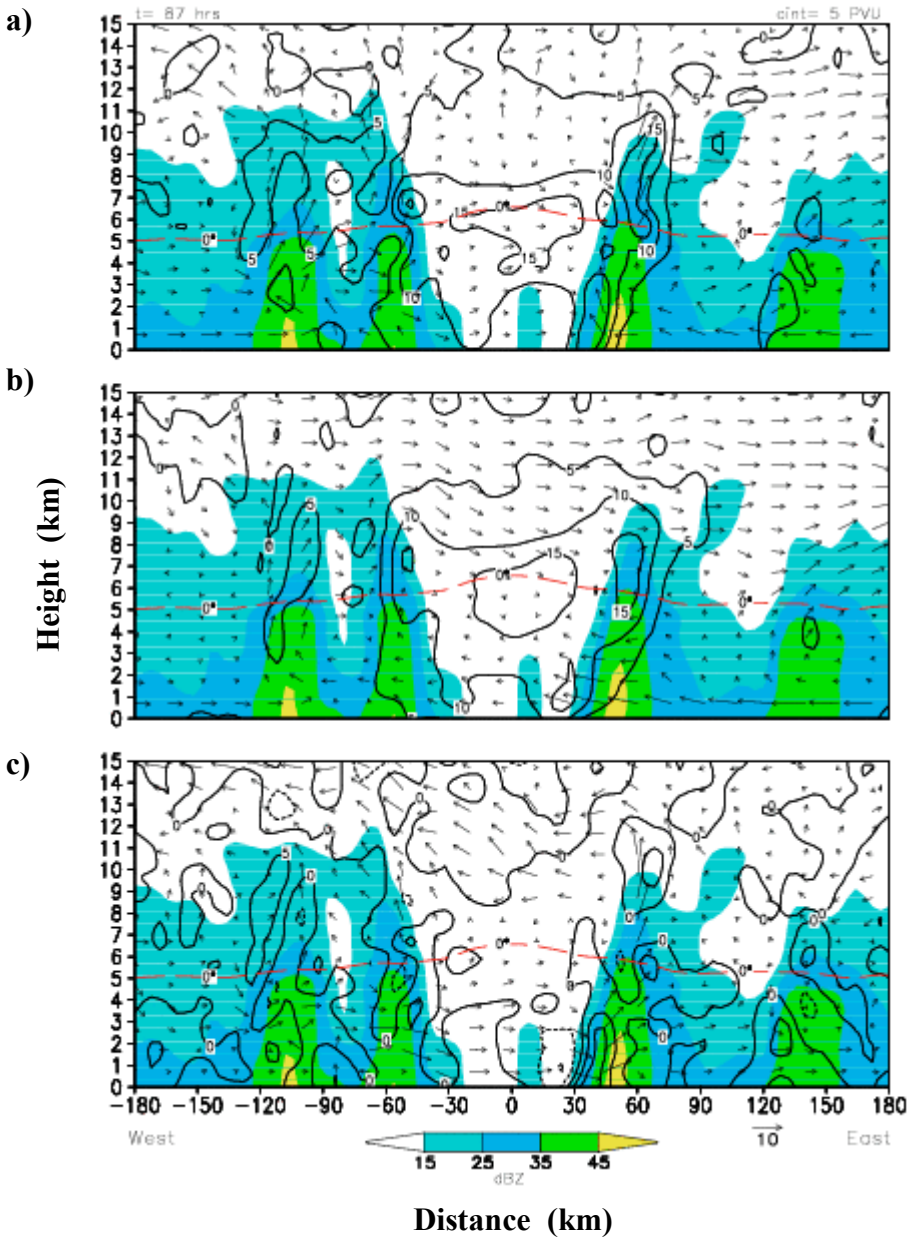

Figure 6. As in Figure 1, but for PV from the 87-h integration. Note that the vertical velocity vectors have been amplified by a factor of 10.

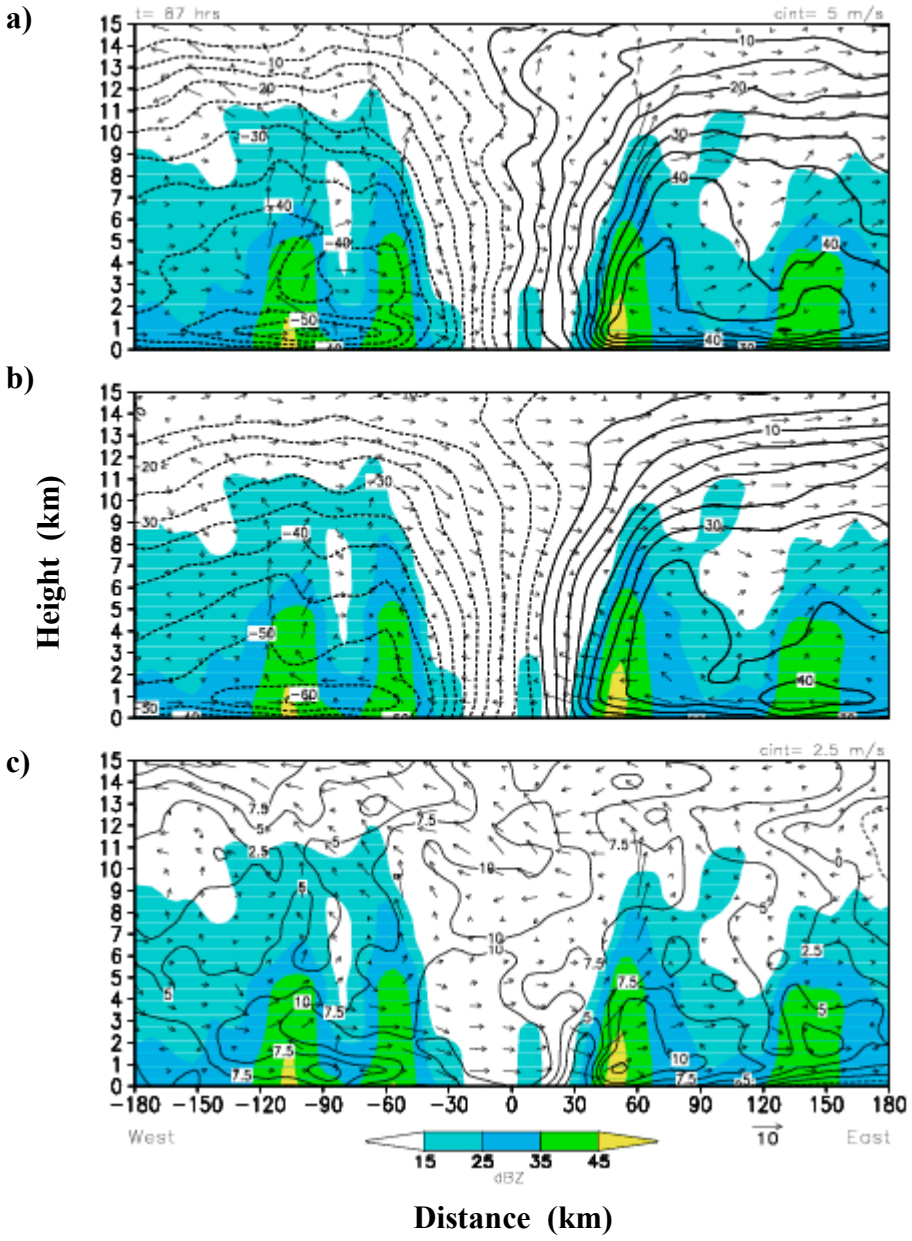

Figure 7. As in Figure 6, but for tangential winds at intervals of 5 m s^{-1} in (a) and (b); and 2.5 m s^{-1} in (c).

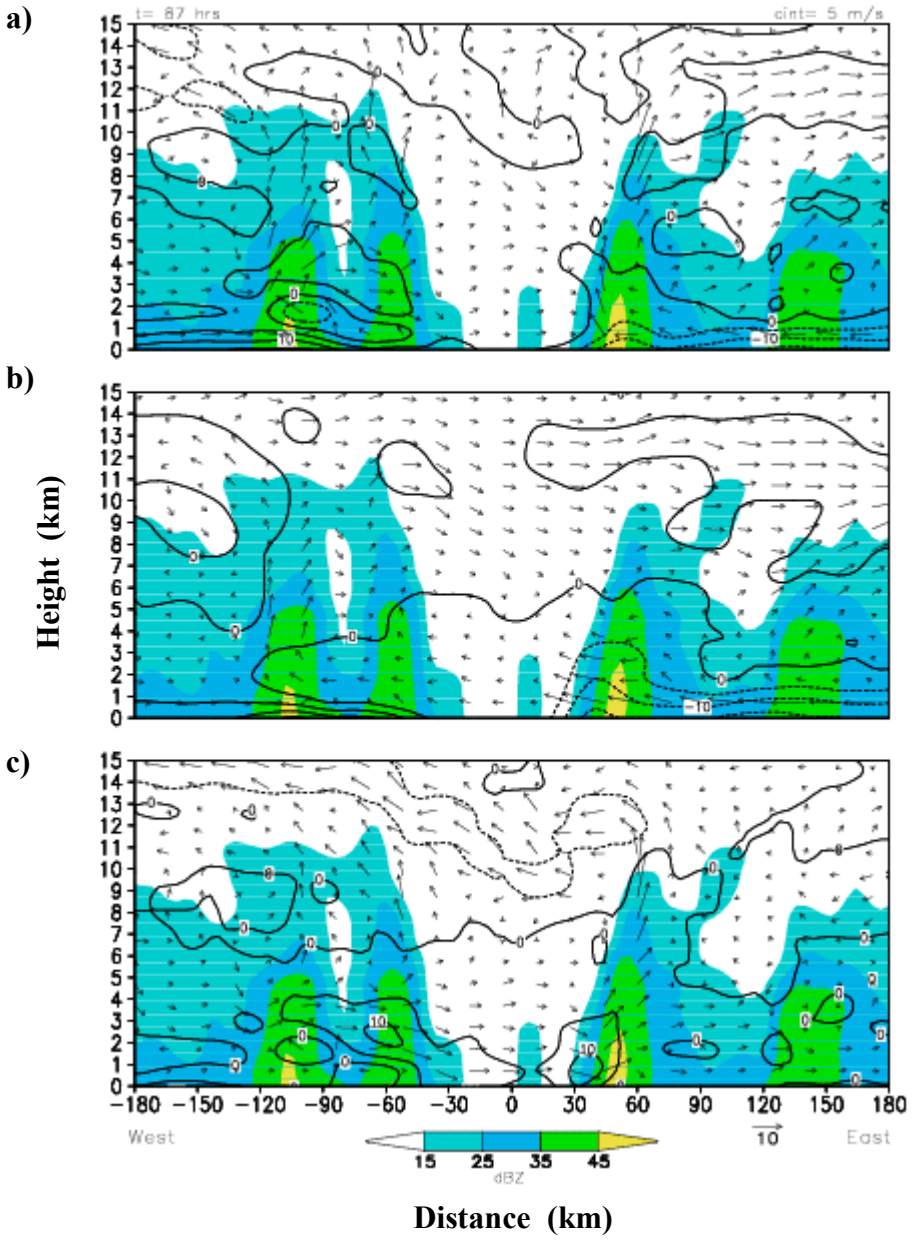

Figure 8. As in Figure 6, but for radial winds at intervals of 5 m s^{-1}.

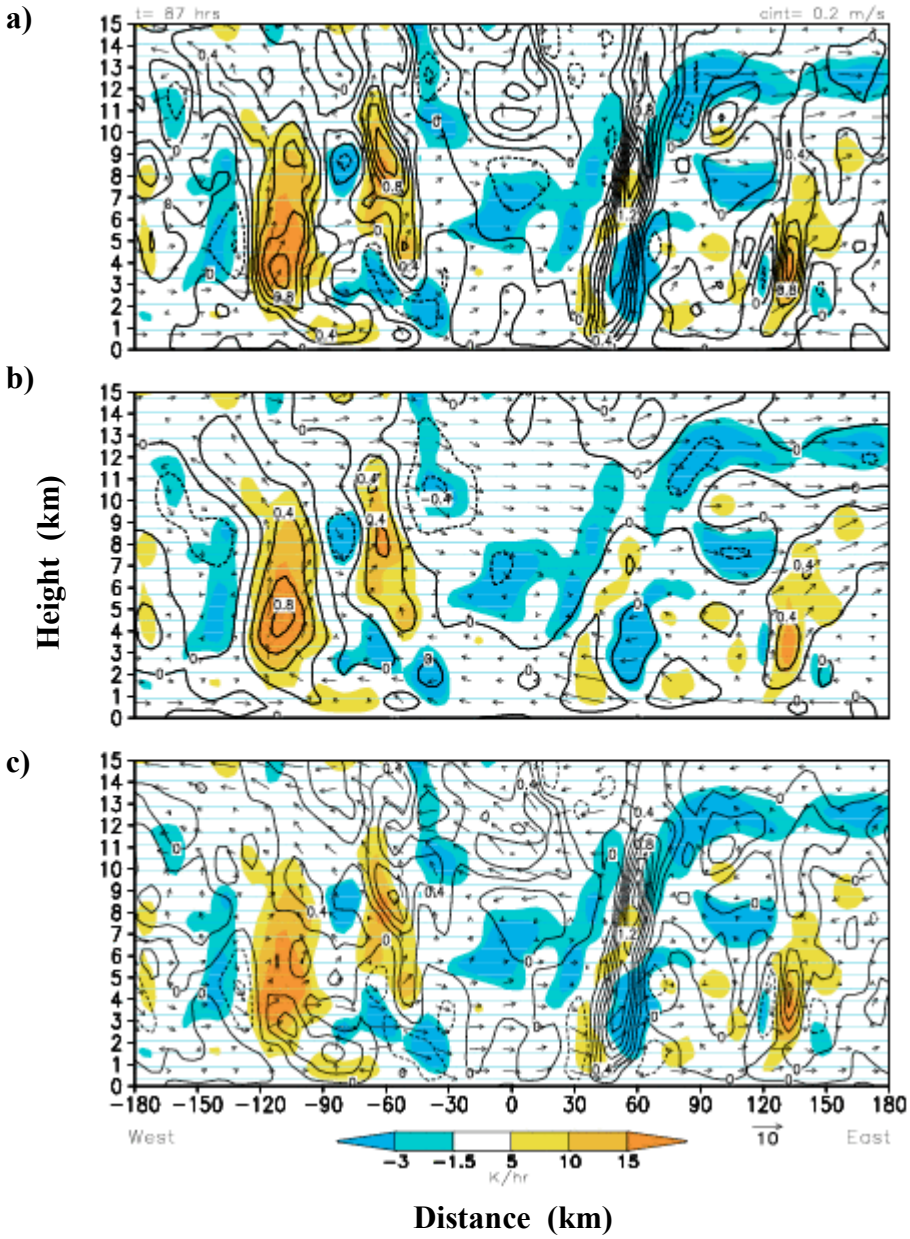

Figure 9. As in Figure 6, but for vertical motions at intervals of 0.2 m s^{-1}. Light shadings denote latent heating rates greater than 5, 10, and 15 K h^{-1}, whereas dark shadings denote latent cooling rates less than -1.5 and -3.0 K h^{-1}.

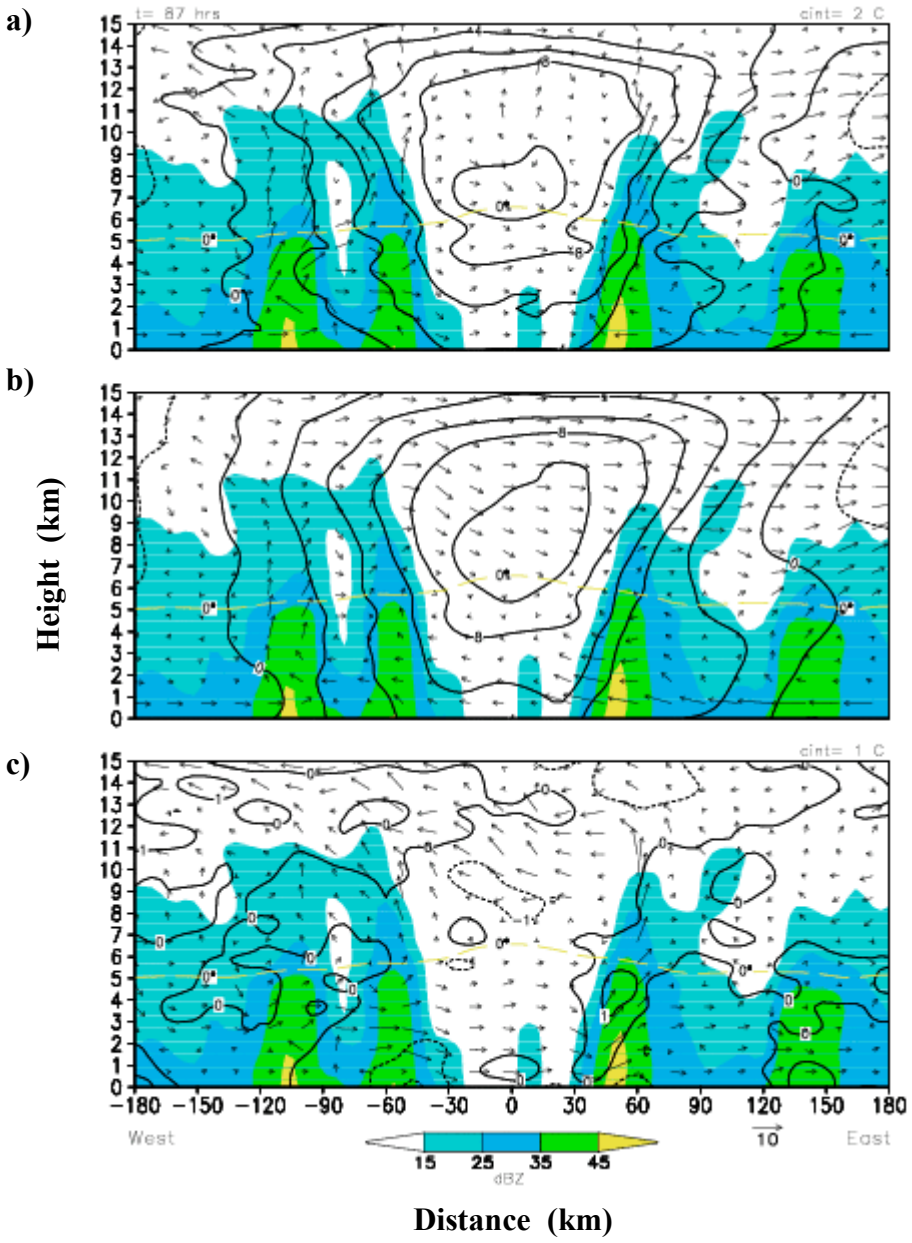

Figure 10. As in Figure 6, but for potential temperature deviations at intervals of 2° C in (a) and (b); and 1° C in (c).